nature communications

Article

https://doi.org/10.1038/s41467-024-53796-z

Toward waterproof magnesium metal anodes by uncovering water-induced passivation and drawing water-tolerant interphases

Received: 7 November 2023

Accepted: 21 October 2024

Yuanjian Li[1], Xiang Feng[2], Gaoliang Yang[1], Wei Ying Lieu[1,3], Lin Fu[4], Chang Zhang[5], Zhenxiang Xing[1], Man-Fai Ng[6], Qianfan Zhang[2], Wei Liu[5] ✉, Jun Lu[7] ✉ & Zhi Wei Seh[1] ✉

Magnesium (Mg) metal is a promising anode candidate for high-energy and cost-effective multivalent metal batteries, but suffers from severe surface passivation in conventional electrolytes, especially aqueous solutions. Here, we uncover that MgH_2, in addition to the well-known MgO and $Mg(OH)_2$, can be formed during the passivation of Mg by water. The formation mechanism and spatial distribution of MgH_2, and its detrimental effect on interfacial dynamics and stability of Mg anode are revealed by comprehensive experimental and theoretical investigations. Furthermore, a graphite-based hydrophobic and Mg^{2+}-permeable water-tolerant interphase is drawn using a pencil on the surface of Mg anodes, allowing them to cycle stably in symmetric (> 900 h) and full cells (> 500 cycles) even after contact with water. The mechanistic understanding of MgH_2-involved Mg passivation and the design of pencil-drawn waterproof Mg anodes may inspire the further development of Mg metal batteries with high water resistance.

With large theoretical capacity (3833 mAh cm^{-3}), low redox potential (−2.37 V vs. standard hydrogen electrode), high abundance in the Earth's crust (ranked 7th of all the elements), and dendrite-resistant nature, magnesium (Mg) metal is considered as a promising anode choice for next-generation high-energy-density, sustainable, and safe batteries[1–4]. However, magnesium metal batteries suffer from unsatisfactory rechargeability owing to severe Mg passivation in conventional non-aqueous electrolytes[5–8]. With progressive studies of Mg battery chemistry, the presence of water contaminants has been demonstrated to be one of the most critical factors for Mg-electrolyte interface passivation[9–11]. On the one hand, trace water (>20 ppm) can change electrolyte solvation structure by competitively solvating complexes to preferentially decompose Mg^{2+}-anion ion pairs, contributing to the passivating interphases on the Mg metal electrode surface[12–15]. On the other hand, water can directly attack Mg metal to generate a passivating surface layer of magnesium oxides (MgO) and hydroxides ($Mg(OH)_2$), which inevitably causes ultrahigh overpotential for reversible Mg plating/stripping[16,17]. Many strategies have been proposed for mitigating the detrimental effect of H_2O, such as introducing water-reactive scavengers[18–21] in traditional electrolytes to

---

[1]Institute of Materials Research and Engineering (IMRE), Agency for Science, Technology and Research (A*STAR), 2 Fusionopolis Way, Innovis #08-03, Singapore 138634, Republic of Singapore. [2]School of Materials Science and Engineering, Beihang University, 100191 Beijing, P. R. China. [3]Pillar of Engineering Product Development, Singapore University of Technology and Design, 8 Somapah Road, Singapore 487372, Republic of Singapore. [4]School of Chemistry and Chemical Engineering, Guizhou University, Guiyang, Guizhou 550025, P. R. China. [5]School of Physical Science and Technology, ShanghaiTech University, Shanghai 201210, P. R. China. [6]Institute of High Performance Computing (IHPC), Agency for Science, Technology and Research (A*STAR), 1 Fusionopolis Way, #16-16 Connexis, Singapore 138632, Republic of Singapore. [7]College of Chemical and Biological Engineering, Zhejiang University, Hangzhou 310027, P. R. China. ✉e-mail: liuwei1@shanghaitech.edu.cn; junzoelu@zju.edu.cn; sehzw@imre.a-star.edu.sg

remove moisture impurities and constructing artificial solid electrolyte interphase (SEI) layers[22,23] to avoid the direct contact between Mg metal and water-containing electrolytes. Despite the exciting research progress, it is still a non-trivial task to develop waterproof Mg metal anodes capable of working stably after direct contact with water, owing to the lack of comprehensive understanding of the mechanism of water-induced Mg passivation.

Accurate identification of the composition of SEI or passivation layers is crucial for the comprehensive understanding of the failure mechanism of alkali and alkaline earth metal anodes. In terms of lithium-metal anode, a particularly contentious issue concerns the existence of lithium hydride (LiH) in the SEI layers[24–27]. By using various advanced characterizations, several independent studies have confirmed that LiH is one of the major components of the SEI layers, and its formation is highly associated with the generation of gases from intrinsic parasitic reactions between metallic Li and electrolytes[24,25]. Due to its poor electronic conductivity and brittle nature, LiH is often regarded as being detrimental to the stabilization of the SEI layer on Li metal anodes[26,27]. In contrast, the high Li ion conductivity of LiH is possibly conducive to boosting Li diffusion kinetics toward favorable Li plating[28]. Massive efforts have also been devoted to investigating the formation of sodium hydride (NaH) in the SEI layers and its controversial role in sodium anode failure[29,30]. Unlike the tremendous progress that has been made in the field of alkali metal hydrides, the investigation of magnesium hydride (MgH_2) is still in a very early phase of research. Recently, Xu et al. reported that MgH_2 could be reversibly formed on the copper selenide (CuSe) cathode in an aqueous carbonate-based electrolyte, aiding the Mg-CuSe batteries in achieving high energy density via the Mg-H^+ energy storage mechanism[31]. However, the role and formation mechanism of MgH_2 on Mg metal anodes remains a poorly understood topic.

In this work, we uncover that, besides well-known $Mg(OH)_2$ and MgO, MgH_2 is also formed in the water-induced surface passivation layer on Mg metal anode. It is demonstrated that water-induced passivation of Mg anode is accompanied by the hydrogen evolution reactions (Eqs. (1), (2)), and more importantly, the released gases can further react with Mg metal (Eq. (3)) to form MgH_2 (Fig. 1a). The spatial distribution of MgH_2 in the $Mg(OH)_2$- and MgO-rich passivation layer is visualized by using time-of-flight secondary ion mass spectrometry (TOF-SIMS). Theoretical calculations indicate that MgH_2, $Mg(OH)_2$, and MgO are all poor in Mg^{2+} adsorption and subsequent transport, and their coexistence in the passivation layer further triggers an intense concentration polarization at the electrode/electrolyte interface, ultimately causing high overpotential (>2 V) and rapid failure (<1 cycle) of water-attacked Mg metal. Accordingly, we propose a facile strategy to enable waterproof Mg anodes by simply drawing graphite-based anti-passivation interphase with a pencil (Fig. 1b). The pencil-drawn graphite (PDG) interphase is not only inherently hydrophobic to protect the underlying Mg metal from water invasion and subsequent passivation, but also exhibits strong magnesiophilicity and high Mg^{2+} diffusivity for low overpotential and reversible Mg plating/stripping behavior. As a result, even after water treatment, the PDG-Mg anode can still operate steadily for over 900 h in a symmetric cell and over 500 cycles in the full cell using a Chevrel phase Mo_6S_8 cathode. The practicability of the waterproof PDG-Mg anode is also extended to a simple aqueous electrolyte.

$$Mg + 2H_2O \rightarrow Mg(OH)_2 + H_2; \Delta H_{calculated} = -359.1\,kJ/mol \tag{1}$$

$$Mg + H_2O \rightarrow MgO + H_2; \Delta H_{calculated} = -285.9\,kJ/mol \tag{2}$$

$$Mg + H_2 \rightarrow MgH_2; \Delta H_{calculated} = -86.0\,kJ/mol \tag{3}$$

Results

Preparation and characterization of the waterproof PDG-Mg electrode

Figure 2a shows the optical image of metallic Mg foil after modification by simply drawing a graphite-based interface layer with a pencil. Benefiting from the solvent-free transfer of the PDG interphase from the pencil to the Mg foil, a large size ($6.5 \times 6\,cm^2$) of PDG-Mg foil can be obtained, holding great promise for large-scale production to meet industrial demands. Considering the homogeneity of microstructure and the efficient protection for Mg metal substrate (Fig. S1), the optimal PDG interphase layer has a mass loading of $0.2\,mg\,cm^{-2}$. To investigate the structural properties of PDG interphase, X-ray diffraction (XRD), Raman spectroscopy, and X-ray photoelectron spectroscopy (XPS) measurements were performed. Compared with the pristine Mg, the PDG-Mg electrode exhibits an additional peak at 26.4° in the XRD pattern

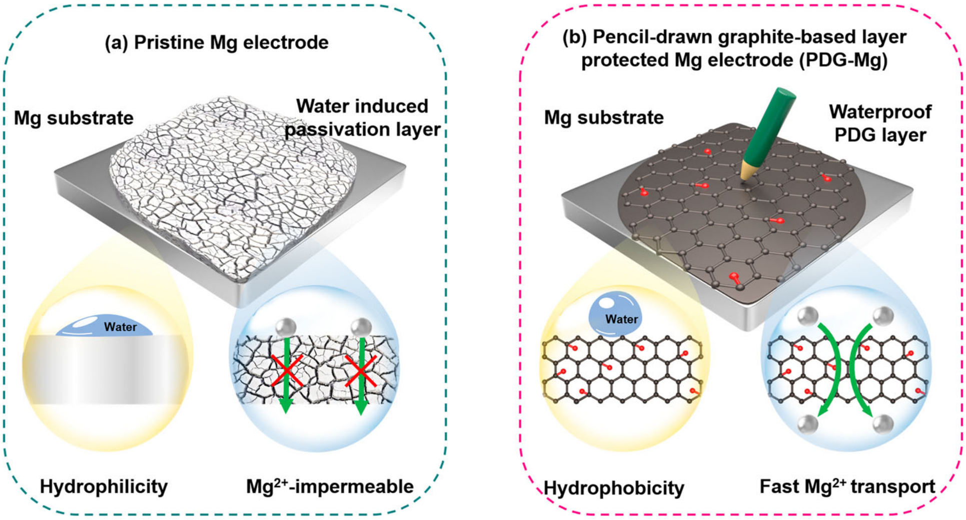

Fig. 1 | Schematic illustration of the water-induced Mg passivation and design concept of waterproof Mg electrode by pencil drawing. a Pristine Mg electrode. Due to the high hydrophilicity, Mg metal is subject to intense water invasion and side effects of gas production, resulting in the formation of a surface passivation layer consisting of $Mg(OH)_2$, MgO, and MgH_2 that blocks Mg^{2+} transport on the anode surface. **b** PDG-Mg electrode. Benefiting from the inherent hydrophobicity, high conductivity, and rapid Mg^{2+} diffusivity, the PDG protective layer not only protects the Mg foil from side reactions related to water but also promotes fast and uniform Mg^{2+} transport during electrochemical cycling.

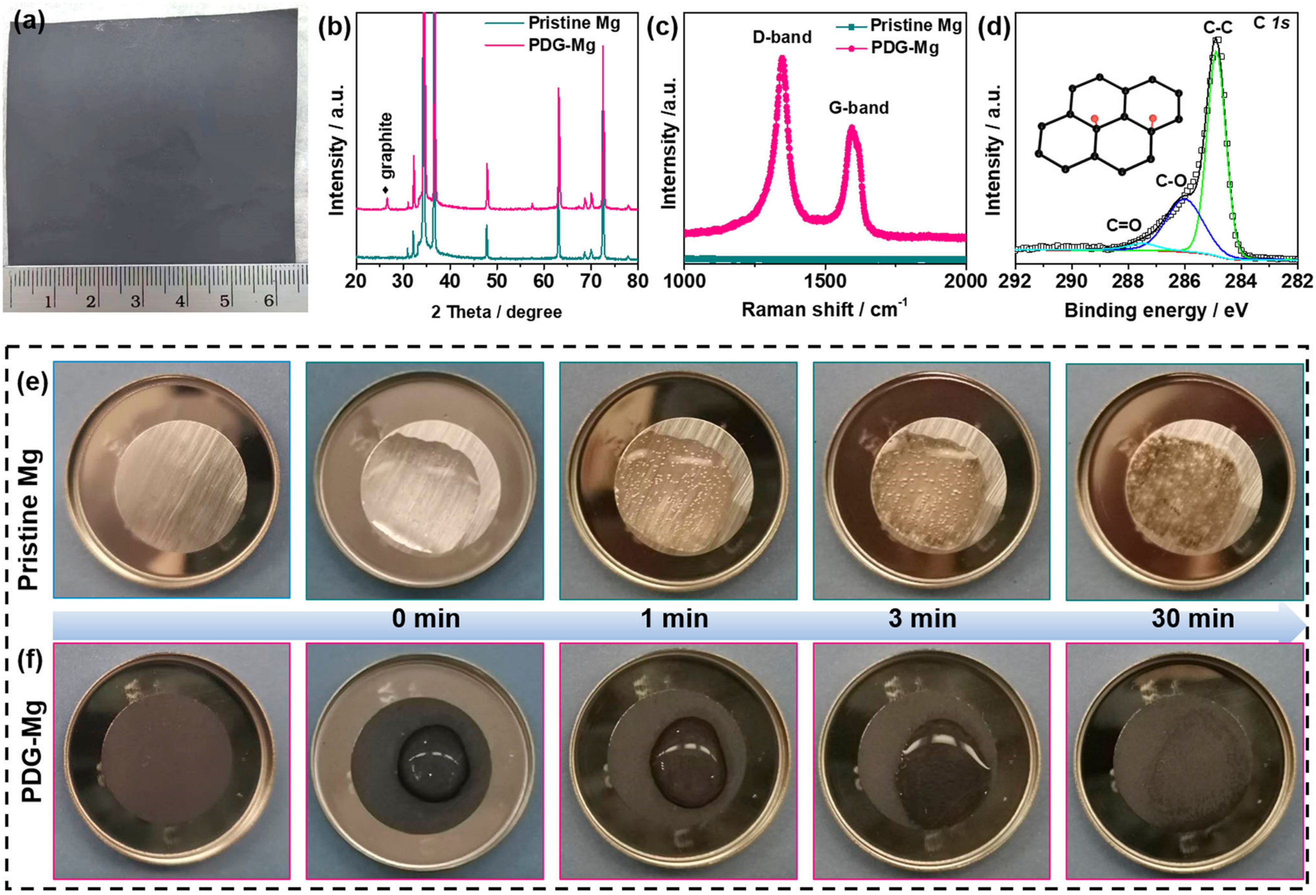

Fig. 2 | Visualizing water-induced Mg passivation and its inhibition by the PDG interphase. a Optical image of large-size of PDG-Mg foil. **b** XRD patterns and (**c**) Raman spectrum of pristine Mg and PDG-Mg electrode. **d** High-resolution C *1s* XPS spectrum of PDG-Mg electrode. Photographs showing water wetting behavior on (**e**) pristine Mg and (**f**) PDG-Mg electrodes during the water treatment.

(Fig. 2b), which corresponds to the (002) plane of graphite[32–34]. The graphitic nature of the PDG interphase is further substantiated through Raman spectroscopy, as shown in Fig. 2c, which reveals characteristic peaks corresponding to the D and G bands at approximately 1350 and 1580 cm^{-1}, respectively. Notably, the intensity of the D-band surpasses that of the G-band, indicative of the high degree of disorder within the PDG structure, stemming from the exfoliation of pencil lead during the drawing process[32]. As observed from the XPS survey spectrum (Fig. S2a), the main elements in the PDG layer are C, O, and Si, respectively. The minimal Si signal (Fig. S2d) likely originates from the SiO_2 clay added during the pencil-lead manufacturing procedure[33]. In the high-resolution C *1s* spectrum (Fig. 2d), three deconvoluted peaks at 284.6, 286.0, and 287.6 eV correspond to graphite C, -C-O, and -C = O groups, respectively. These O-containing groups are also evident in the O *1s* spectrum (Fig. S2c) and often play a pivotal role in improving the surface metallophilicity of carbon-based materials[35].

Visualizing water-induced Mg passivation and its inhibition by PDG interphase

After successfully synthesizing the PDG interphase, our initial experimental investigation focused on assessing its effectiveness in mitigating water intrusion onto the underlying Mg metal. Figure 2e, f provide a series of time-lapse optical images depicting the behavior of pristine Mg and PDG-Mg electrodes upon adding a droplet (30 μL) of water to their surfaces. Upon contact with water, the pristine Mg electrode rapidly becomes wetted, showcasing its inherent hydrophilic nature. Simultaneously, some bubbles are visible on the pristine Mg electrode attributed to the hydrogen evolution reaction. Along with gas evolution, pristine Mg foil begins to lose its metallic luster after 1 min of water treatment. As the water treatment progresses, the surface of the pristine Mg electrode ultimately transitions into an uneven greyish-white appearance, signifying substantial electrode passivation. In stark contrast, when water droplets contact the surface of the PDG-Mg electrode, they exhibit minimal spreading, and no bubbles are generated throughout the entire water treatment process. This waterproof behavior can be attributed to the distinctive characteristics of the PDG interphase, which not only affords hydrophobicity to suppress the spreading of water droplets, but also serves as a shield, preventing water from permeating through and initiating detrimental side reactions with the underlying Mg substrates.

Identification of the chemical composition of water-induced passivation layer

To investigate the structural changes occurring on the surfaces of both pristine Mg and PDG-Mg electrodes during water treatment, we employed scanning electron microscopy (SEM) and energy-dispersive X-ray spectroscopy (EDX). In Fig. 3a, b, it is evident that the pristine Mg electrode undergoes a transformation from a smooth surface to one that is porous and rough following water treatment. Additionally, the EDX spectrum reveals a notable increase in the presence of O element (Fig. S3). These observations provide compelling evidence of severe passivation affecting the pristine Mg electrode, a conclusion corroborated by the appearance of peaks corresponding to $Mg(OH)_2$ and MgO in the XPS spectra and XRD patterns (Fig. S4)[17]. To accuratly identify the chemical components and their spatial distribution within the water-induced passivation layer, TOF-SIMS and Raman measurements were

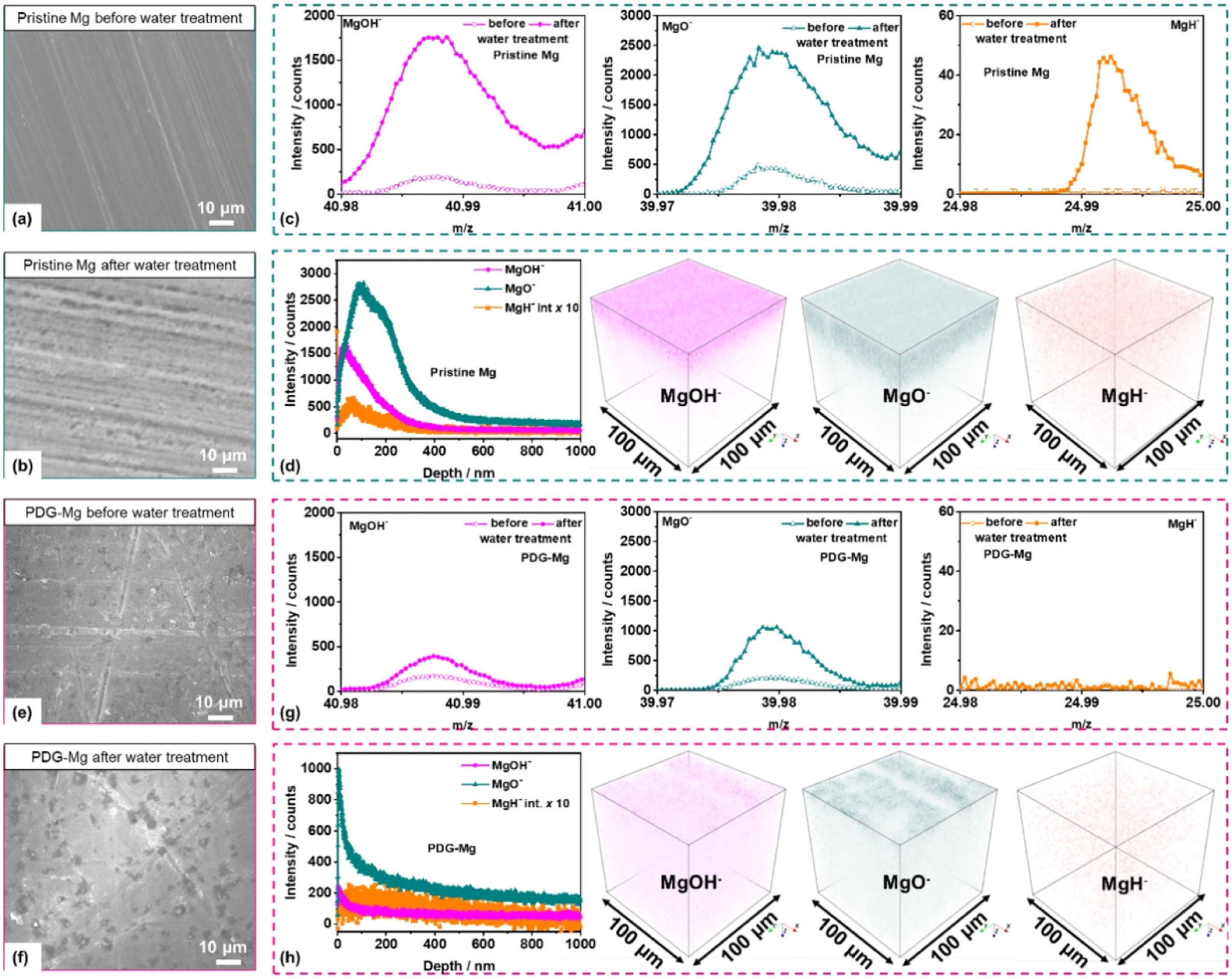

Fig. 3 | Identification of the chemical composition of the water-induced passivation layer. a, **b** SEM images and (**c**) TOF-SIMS spectra of MgOH$^-$, MgO$^-$, and MgH$^-$ ion obtained from pristine Mg electrode before and after 30 mins of the water treatment. **d** TOF-SIMS depth profiles and 3D render images of MgOH$^-$, MgO$^-$, and MgH$^-$ for pristine Mg electrodes after 30 min of the water treatment. **e**, **f** SEM images and (**g**) TOF-SIMS spectra of MgOH$^-$, MgO$^-$, and MgH$^-$ ion obtained from PDG-Mg electrode before and after the water treatment. **h** TOF-SIMS depth profiles and 3D render images of MgOH$^-$, MgO$^-$, and MgH$^-$ for PDG-Mg electrodes after 30 min of the water treatment.

further performed on pristine Mg after the water treatment. As displayed in Fig. 3c, Fig. S9, ion fragments of MgOH$^-$, MgO$^-$, and MgH$^-$ are detected at the mass-to-charge ratio (m/z) = 40.988, 30.978, and 24.995, respectively, which can be attributed to $Mg(OH)_2$, MgO, and MgH_2 products. In particular, the signal intensity of MgH$^-$ is approximately an order of magnitude weaker than that of MgOH$^-$ and MgO$^-$, which might explain why previous studies did not detect MgH_2, potentially leading to its oversight. From the depth profile of the pristine Mg electrode after 30 mins of water treatment (Fig. 3d), we also observed an intensity peak of MgH$^-$ at a depth of approximately 50 nm, providing solid evidence for the existence of MgH_2. In addition, the MgO$^-$ signal remains detectable throughout the entire etching process, indicating that the thickness of the passivation layer likely exceeds 1 µm. 3D reconstructions of these detected signals were further provided to gain further insight into the microstructure of the passivation layer (Fig. 3d). It can be clearly observed that MgOH$^-$ and MgO$^-$ are densely concentrated within the outermost 100 nm and 300 nm, respectively, while the MgH$^-$ signal is sparsely distributed throughout the passivation layer. The Raman spectra of the water-treated pristine Mg electrode (Fig. S10b) also exhibits characteristic MgO bands at 278 and 445 cm^{-1}[36], MgH_2 band at 311 cm^{-1}[31], and $Mg(OH)_2$ bands at 725 and 810 cm^{-1}[37], which again evidence the co-existence of MgH_2, $Mg(OH)_2$, and MgO in the water-induced passivation layer on metallic Mg. It's also worth noting that no MgH_2 signal can be detected from the pristine Mg foil before use and after 30 min of air exposure (Fig. S10), which in turn illustrates that the formed MgH_2 originates from the side reactions with Mg and H_2O during the water treatment (see Eqs. (1)–(3)).

Prior to water treatment, the surface of the PDG-Mg electrode exhibits a relatively rough texture, featuring the distribution of numerous flakes, as depicted in Fig. 3e and Fig. S7a. A closer examination using transmission electron microscopy (Fig. S7b) reveals that these flakes have dimensions on the order of several hundred nanometers, displaying the characteristic two-dimensional structure associated with multilayer graphite[32,33]. A cross-sectional view (Fig. S7c, d) highlights the close connection between the PDG interface layer and the underlying Mg substrate, with the thickness of the PDG interphase measuring approximately 1 µm. Under the protective shield of this PDG interphase, the PDG-Mg electrode showed minimal changes in the surface morphologies after the same water treatment (Fig. 3f). The compositional features of PDG-Mg electrode before and after the water treatment was further compared by the results of TOF-SIMS, EDX, XPS, XRD, and Raman spectroscopy, as displayed in Fig. 3g, h, and Fig. S8–10. It can be clearly observed that the graphitic nature of the PDG interphase remains almost unchanged except for a slight increase in the O signal, which should comes from the MgO and $Mg(OH)_2$ that forms during the water treatment. More importantly, the water-induced by-product, MgH_2, is undetectable from the PDG-Mg electrode during the whole water treatment process. Based on above comprehensive characterisations, it can be validated that the side reactions between Mg and water is greatly prevented with the protection of the PDG interphase.

Probing the working mechanism of the passivation layer and the PDG interphase

After identifying the chemical components within the water-induced passivation layer, we conducted first-principles calculations to understand their effects on the interfacial kinetics and stability of the Mg metal anode. As exhibited in Fig. 4a, the band gap of MgH_2, $Mg(OH)_2$, and MgO is calculated to be 4.05, 6.38, and 6.02 eV, respectively. The lower band gap of MgH_2 suggests that MgH_2 formed in the passivation layer can increase the electron tunneling probability from the Mg metal substrates to the electrolytes, thus promoting further side reactions between them[36,37]. Additionally, MgH_2 also exhibits a significantly lower electrochemical stability window (ESW, 0.43 V, Fig. 4b) compared to $Mg(OH)_2$ (2.02 V), MgO (3.05 V), and other magnesium compounds (0.75–5.74 V). These results further underscore that the existence of MgH_2 in the passivation layer may adversely affect the stability of the electrode/electrolyte interface.

Density functional theory (DFT) calculations were further applied to delve deeper into the interactions between the passivation layer and H_2O molecules or Mg atoms. The adsorption models on the surfaces of $MgH_2(001)$, $Mg(OH)_2(001)$, and MgO(001) were summarized in Fig. S11, S12. It can be seen from Fig. 4c that the adsorption energy of H_2O is greater than that of Mg on all the surfaces: MgH_2 (−1.03 eV for H_2O vs. −0.50 eV for Mg), $Mg(OH)_2$ (−0.48 eV for H_2O vs. −0.47 eV for Mg), and MgO (−0.77 eV for H_2O vs. −0.52 eV for Mg). These values indicate the hydrophilic and magnesiophobic properties of the passivation layer, which is likely to induce an H_2O-rich and Mg^{2+}-poor region in the vicinity of electrode, seriously exacerbating further side reactions between passivated Mg anode and aqueous solutions. Conversely, the O-containing graphite in the PDG layer exhibits a much stronger interaction with Mg adatom (−1.62 eV) as compared to H_2O (−0.28 eV), which favors the establishment of a region of Mg enrichment and H_2O depletion near the PDG-Mg anode, thus allowing reversible Mg plating/stripping behavior in liquid electrolytes, including aqueous solutions.

Figure 4d visualizes the differential charge density of the most stable configurations for MgH_2, $Mg(OH)_2$, MgO, and O-containing graphite with Mg adatoms adsorption. The electron of the adsorbed Mg atom on the O-containing surface groups of the PDG layer is more delocalized, contributing to the stronger interfacial interactions between them. Furthermore, as revealed by Bader charge, the electron donation of Mg to O-containing graphite reaches 0.9 e, much higher than those of MgH_2 (0.1 e), $Mg(OH)_2$ (0.5 e), and MgO (0.2 e), suggesting a stronger magnesium affinity of PDG interphase. Together with its metallic-like conductivity[34], PDG interphase plays a crucial role in alleviating Mg depletion and mitigating voltage hysteresis during Mg electroplating.

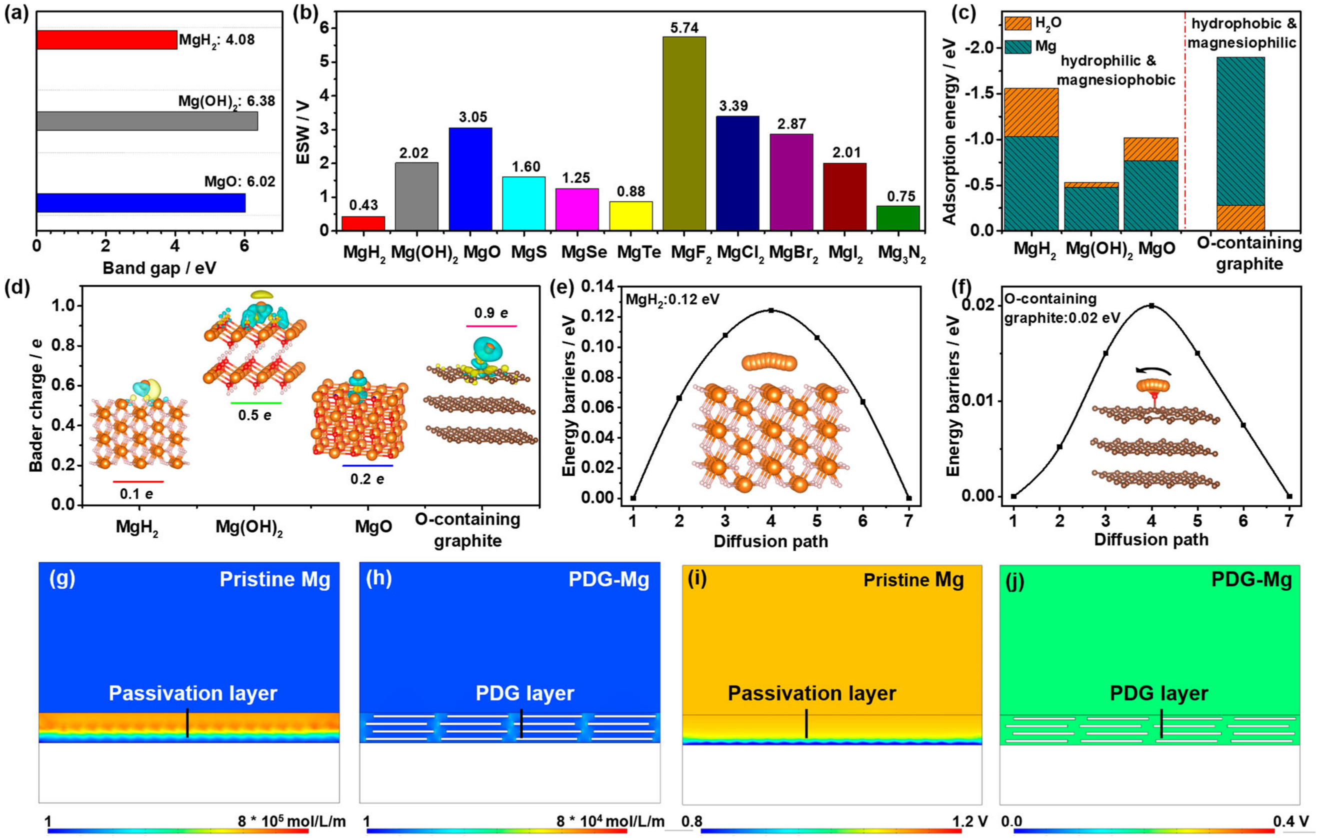

Fig. 4 | Theoretical investigation of the working mechanism of the water-induced passivation layer and the waterproof PDG layer. The comparison of (**a**) band gap and (**b**) electrochemical stability window of MgH_2 with $Mg(OH)_2$ and MgO. **c** DFT adsorption energies of H_2O molecules and Mg adatoms on $MgH_2(001)$, $Mg(OH)_2(001)$, MgO(001), and O-containing graphite. **d** Charge density difference plots, and Bader charge of Mg adatom on $Mg(OH)_2(001)$, MgO(001), $MgH_2(001)$, and O-containing graphite. Blue and yellow spheres indicate charge depletion and accumulation regions, respectively. The calculated Mg diffusion energy barrier on (**e**) MgH_2 and (**f**) O-containing graphite. The orange, red, and brown balls denote Mg, O, and C elements, respectively. COMSOL simulation of the distribution of (**g**, **h**) Mg^{2+} concentration and (**i**, **j**) electric field over the Mg anode surface with (**g**, **i**) the passivation layer and (**h**, **j**) the PDG interphase at a current density of 1 mA cm^{-2}.

In addition to its hydrophobic and magnesiophilic properties, the PDG interphase is also conducive to facilitating Mg ion transport, a critical factor for the success of a Mg protective layer. Utilizing the climbing-image nudged elastic band (CI-NEB) method, we have calculated that the energy barrier for Mg diffusion on the O-containing graphite is exceptionally low, measuring just 0.02 eV (Fig. 4e). This value stands in stark contrast to the higher barriers observed for MgH_2 (0.17 eV, Fig. 4f), MgO (0.2 eV, Fig. S13a), and $Mg(OH)_2$ (0.03 eV, Fig. S13b), clearly indicating a significantly faster Mg transport through the PDG interphase compared to conventional passivation layers. Furthermore, the confined liquid electrolyte in the gaps between the pencil-drawn graphite sheets also allows rapid Mg transportation on the PDG-Mg surface. Benefiting from the dual enhancement of Mg-transfer capability and magnesiophilicity by the PDG interphase, the Mg electroplating behavior on the anode surface is expected to be significantly improved.

To validate our previous hypothesis, we conducted simulations of ion flux distribution and electric field across the Mg anode surface using finite element simulations through COMSOL Multiphysics[38,39]. The simulation models (Fig. S14) were built by introducing a compact passivation layer and stacked graphite flakes onto the surfaces of pristine Mg and PDG-Mg electrodes, respectively. Due to the inherent poor affinity of Mg and the substantial diffusion barrier for Mg ions, the concentration of Mg^{2+} ions near the passivated surface of pristine Mg electrode can be observed to be notably lower than that in the bulk electrolyte (Fig. 4g, Fig. S15). This marked concentration polarization at the Mg/electrolyte interface enhances the surrounding electric field intensity, as depicted in Fig. 4i. Consequently, it leads to a significant increase in overpotential and diminished reversibility during Mg plating and stripping. Encouragingly, with the introduction of the PDG surface layer, we witnessed a substantial enhancement in Mg^{2+} concentration, soaring from 1.55 to 480 mol m^{-3} (Fig. 4h, Fig. S15). Simultaneously, there was a sharp reduction in overpotential, declining from 1.05 to 0.20 V (Fig. 4j). Most importantly, the presence of the PDG interphase led to the uniformization of both the Mg^{2+} flux and the electric field at the electrode/electrolyte interface, accounting for achieving highly reversible and low-barrier Mg plating.

Electrochemical performance of the PDG-Mg electrodes after the water treatment

To assess the practicality of the waterproof PDG-Mg electrodes, we conducted galvanostatic cycling tests on symmetric cells employing PDG-Mg electrodes following water treatment (achieved by adding 30 μL of water to their surfaces). 0.3 M $Mg(OTf)_2$ and 0.2 M $MgCl_2$ in DME was chosen as the electrolyte, as this conventional non-nucleophilic electrolyte is highly compatible with Mg metal electrodes[40–42]. As exhibited in Fig. 5a, the symmetric cell utilizing water-treated pristine Mg anodes initially exhibits pronounced oscillations in the voltage curves, suggesting the deactivation of the pristine Mg electrode due to passivation reactions induced by contact with water. In contrast, the symmetric cell employing the water-treated PDG-Mg electrode demonstrates stable Mg plating/stripping cycling over 900 h at 1.0 mA cm^{-2} and 1.0 mA h cm^{-2}. This endurance implies that the electrochemical activity and stability of PDG-Mg electrodes remain unaffected during the water treatment. Upon closer examination of the enlarged voltage curves, it can be found that the overpotential remains at approximately 200 mV after the first activation cycle and only experiences a slight increase to approximately 250 mV after 900 h of continuous cycling. This consistent, small, and stable overpotential observed in the waterproof PDG-Mg electrode serves as

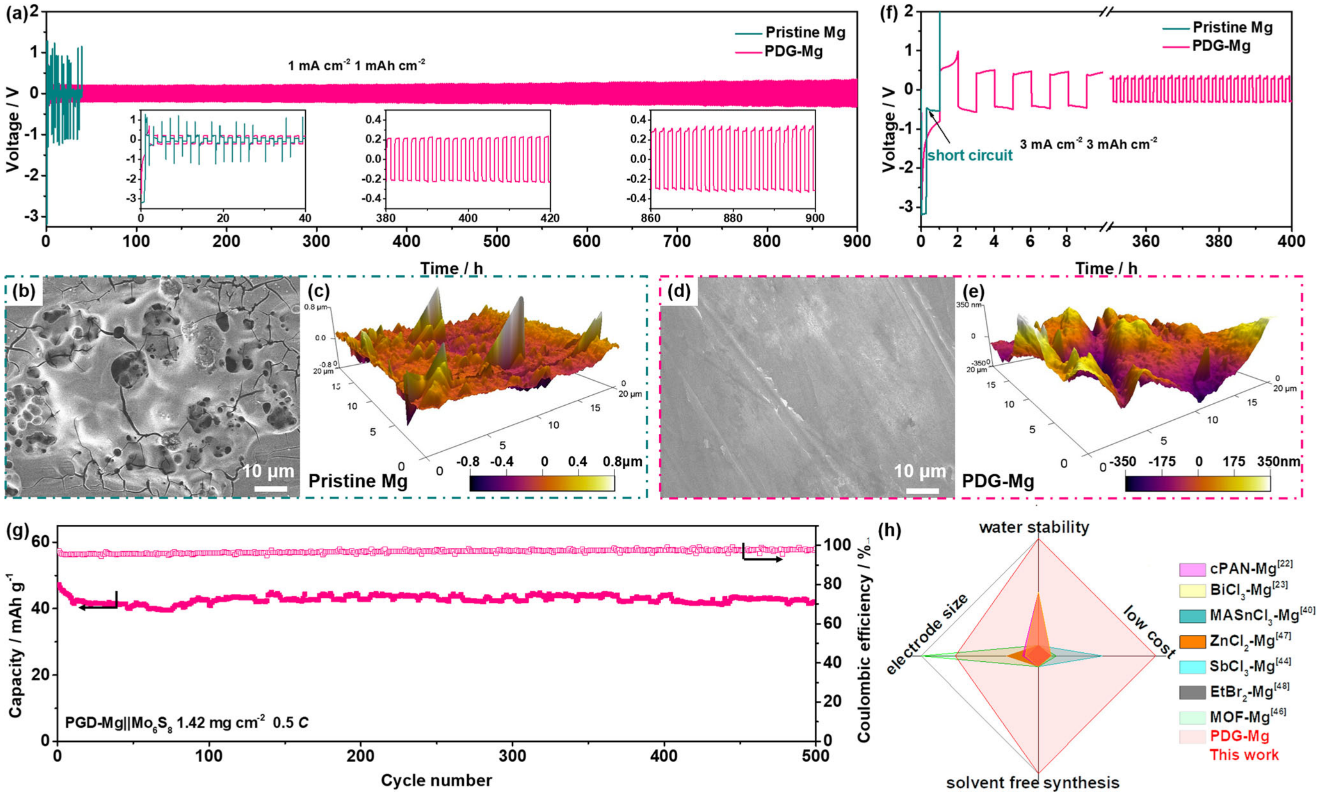

Fig. 5 | Electrochemical performance of the waterproof electrode. **a** Galvanostatic voltage curves of symmetric cells with water-treated pristine Mg or PDG-Mg electrodes in a conventional non-nucleophilic electrolyte at 1.0 mA cm^{-2} and 1.0 mAh cm^{-2} (**b**, **d**) SEM and (**c**, **e**) AFM images of water-treated pristine Mg or PDG-Mg electrodes resulted from the symmetric cells after 10 cycles at 1.0 mA cm^{-2} and 1.0 mAh cm^{-2}. **f** Galvanostatic voltage curves of symmetric cells with water-treated pristine Mg or PDG-Mg electrodes in a conventional non-nucleophilic electrolyte at 3.0 mA cm^{-2} and 3.0 mAh cm^{-2}. **g** Cycling performance of water-treated PDG-Mg||Mo_6S_8 full cell. **h** Comparison of our PDG interphase with other reported artificial interphases as summarized in Table S1.

compelling evidence of the uniqueness of the PDG interphase and its vital role in expediting Mg^{2+} transfer to the Mg anode surface and stabilizing the Mg/electrolyte interface.

Post-mortem SEM, atomic force microscopy (AFM), and XPS investigations were applied to gain further insights into the surface morphology and chemistry of water-treated pristine Mg and PDG-Mg electrodes after cycling in symmetric cells. The SEM image in Fig. 5b suggests that the cycled pristine Mg electrode exhibits a highly porous surface structure with numerous cracks randomly distributed across its surface. Furthermore, an observed height difference of approximately 0.8 µm from the AFM image (Fig. 5c) indicates the accumulation of a substantial number of by-products on the pristine Mg electrode during cycling. Conversely, the PDG-Mg electrode, after 10 cycles, presents a relatively flat and densely packed surface with a height difference of only about 0.35 µm (Fig. 5d, e). Even after cycling for 50 plating/stripping cycles (Fig. S16, 17), the PDG interphase maintains its structural integrity, as evidenced by the presence of C and Si elements in the EDX mappings. From the results of XPS spectra (Fig. S18), the relative intensities of the MgO, $Mg(OH)_2$, and MgF_2 of the PDG-Mg is significantly lower compared with those of the pristine Mg, and the formation of $MgCO_3$, which is poor in Mg^{2+} transport[40], is also eliminated. We also note a distinct peak related to metallic Mg (49.4 eV) in the Mg *2p* XPS spectrum of cycled PDG-Mg electrode[41,42], which further suggests that the PDG-layer can suppress electrolyte decomposition, thus contributing to low interfacial resistance (Fig. S19) for rapid Mg^{2+} electroplating and stripping.

When the cycling current density and areal capacity are raised to 3.0 mA cm^{-2} and 3.0 mAh cm^{-2} (Fig. 5f, Fig. S20), the water-treated Mg||Mg symmetric cell could not run at all. As a comparison, with the PDG interphase protection, stable electrochemical Mg plating/stripping for more than 400 h can be achieved in the water-treated PDG-Mg||PDG-Mg symmetric cell. Furthermore, the water-treated PDG-Mg can also steadily run at a current density up to 5.0 mA cm^{-2} (Fig. S21), indicative of its promising rate capability. To meet the practical requirement, we assembled the full Mg-metal cells using a Chevrel phase Mo_6S_8 cathode to pair with the water-treated PDG-Mg electrode. At a current density of 0.5 *C* (Fig. 5g), the full cell affords an initial capacity of 47.2 mAh g^{-1}, which remains at 42.1 mAh g^{-1} after 500 cycles, corresponding to a capacity retention of 89.2%. Such cycling stability is comparable to that of the full cell utilizing an untreated Mg anode, which achieved a capacity retention of 92.3% after 500 cycles at 0.5 C, as shown in Fig. S22. These results provide solid evidence that the PDG interphase effectively inhibits water-induced passivation and deterioration of the metallic Mg anode. It's also worth noting that the fluctuations in capacity from temperature variation during long-term battery cycling are highly reproducible (Fig. S23) and have been widely observed in literature[7,39,43]. The practicality of the waterproof PDG-Mg electrode was further validated in a 5 M $MgCl_2$ aqueous electrolyte. As illustrated in Fig. S24a, the symmetric cell using PDG-Mg electrodes exhibits long-term stability over 100 h, significantly outperforming its pristine Mg counterpart. Moreover, the PDG-Mg||Mo_6S_8 full cell also achieves relatively stable cycling performance (Fig. S24b).

To put this work in a historical perspective, we summarized the previous efforts of constructing artificial interface layers for enabling reversible Mg-metal anode chemistry (Fig. 5h). A notable example is that Ban et al. engineered a thermal-cyclized polyacrylonitrile (cPAN)-based polymeric layer on the Mg powder surface, which enabled the reversible cycling of a high-voltage Mg metal battery with a vanadium pentoxide cathode in the water-containing, carbonate-based electrolyte[22]. Inspired by this work, many other Mg^{2+} conductive layers have been artificially achieved by metal-organic framework coating[44], and inorganic or organic organohalogen compounds modification[23,38,42,45,46]. However, the effectiveness of these artificial layers against the water instability of the Mg metal anode remains unexplored. Moreover, the PDG-Mg electrode without water treatment is also capable of cycling stably in $Mg(OTf)_2$-$MgCl_2$-DME electrolyte with H_2O addtives (Fig. S24), and even in a chloride-free magnesium bis(trifluoromethanesulfonimide) ($Mg(TFSI)_2$)-DME electrolyte (Fig. S26), showcasing the advantages of PDG interphase in realizing reversible Mg-metal anode chemistry. Taking other factors into consideration, listed in Table S1, including low cost, electrode size, and solvent-free synthesis of PDG interphase, it is reasonable to expect that our PDG-Mg electrode holds great promise toward the development of affordable and practical Mg metal batteries.

Discussion

In summary, we uncover the water-induced Mg passivation mechanism and showcase that water can react readily with Mg metal to generate MgO and $Mg(OH)_2$, meanwhile, the released H_2 will further passivate the Mg metal through the formation of MgH_2. The spatial distribution of MgO, $Mg(OH)_2$, and MgH_2 in the passivation layer is revealed by TOF-SIMS. We also find that the passivation layer is poor in Mg^{2+} adsorption and subsequent transport, which prevents reversible magnesium plating/stripping on the surface of water-treated Mg electrode. As a proof of concept, a waterproof Mg electrode is successfully developed by drawing a graphite-based anti-passivation interphase on the Mg metal surface with a pencil. With its inherent hydrophobicity, compact structure, high magnesiophilicity, and rapid Mg^{2+} diffusivity, the PDG interphase not only efficiently avoids water invasion into the underlying Mg substrates, but also significantly increases Mg plating/stripping reversibility by homogenizing the distribution of ion flux and electric field at the electrolyte-electrode interface. With such a PDG protective layer, the Mg metal anode, even after water treatment, is still capable of working steadily for over 900 h in symmetric cells and over 500 cycles in full cells using Mo_6S_8 as the cathode. The insights gained from the identification of MgH_2 in the passivation layer, the mechanistic understanding of Mg passivation by H_2O, as well as the construction of anti-passivation interphase pave the way toward the development of waterproof Mg metal anode and other H_2O-sensitive battery chemistries.

Methods

Electrode preparation

The purchased Mg foil (99.9%, 0.1 mm thick, MTI) was first polished by a blade until the surface was shiny to clean surface contaminants. Then the PDG-Mg electrode was prepared by drawing a graphite-based protective layer onto polished Mg foils using a commercial pencil (2B pencil, M&G Chenguang Stationery Co., Ltd.). The average thickness and mass loading of the PDG layer are ~ 2 μm and ~ 0.2 mg cm^{-2}, respectively. After punching into round pieces with a diameter of 12.7 mm, the used PGD-Mg electrode can be obtained.

Electrolyte preparation

The non-aqueous electrolyte was prepared by dissolving 1.5 mmol of magnesium triflate ($Mg(OTf)_2$, 99.5%, Solvionic) and 1 mmol magnesium chloride ($MgCl_2$, ≥98%, Sigma-Aldrich) in 5 mL of 1,2-dimethoxyethane (DME, 99.5%, Sigma-Aldrich). The aqueous electrolyte was prepared by dissolving 5 mmol $MgCl_2$ in 1 mL deionized water.

Characterization

The morphologies of pristine Mg and PDG-Mg electrodes were observed on a JEOL 7600 F scanning electron microscopy (SEM) equipped with an Oxford Technology X-ray detector and FEI Talos f200x transmission electron microscopy (TEM). The surface chemistry of pristine Mg and PDG-Mg electrodes was characterized by X-ray photoelectron spectroscopy (Thermo Fisher Scientific, with Al Kα radiation of 1486.6 eV), X-ray diffraction (Bruker D8 with Cu Kα radiation, λ = 1.5418 Å), Raman spectroscopy (Renishaw 200 system with a 532-nm excitation laser), and time-of-flight secondary ion mass spectrometry (IONTOF GmbH, Germany measurements). The cycled electrodes were disassembled and washed with DME solvent for further analysis in an argon-filled glove box ($H_2O < 0.1$ ppm, $O_2 < 0.1$

ppm). Airtight sample holders were used to transfer samples from the glove box to the sample chamber.

Electrochemical measurements

Electrochemical measurements were carried out using CR2032 coin-type cells at room temperature (~ 25 °C). A glass fiber separator (WhatmanTM GF/D) soaked with 80 µL of non-aqueous or aqueous electrolyte was used in each cell. In the case of non-aqueous electrolyte, the cells were assembled or disassembled in an Ar-filled glovebox ($H_2O < 0.1$ ppm, $O_2 < 0.1$ ppm). In the case of aqueous electrolyte, the cells were assembled or disassembled in atmospheric air. For the full cells, Mo_6S_8 was prepared and used as the cathode[40]. The Mo_6S_8 cathode was made by blending Mo_6S_8 power, Super P carbon, and polyvinylidene difluoride binder with a weight ratio of 8: 1: 1 to form the slurry, and then coated on the nickel foil. After drying at 60 °C under vacuum overnight, the obtained electrodes had an areal mass loading controlled to be ~ 1.42 mg cm^{-2}. These full cells were charged/discharged galvanostatically between 0.2 and 2.0 V vs. Mg^{2+}/Mg on the electrochemical test system (Neware, CT-4008T-5V50mA-164, Shenzhen, China). Electrochemical impedance spectroscopy (EIS) was performed by a Gamry electrochemical workstation (Reference 600+) Potentiostat between 100 kHz and 0.1 Hz with a sinusoidal voltage of 5 mV.

DFT calculations

All the simulations are carried out based on Density Functional Theory (DFT)[47], employing the Vienna Ab initio Simulation Package (VASP)[48,49]. The exchange-correlation energy is calculated using the Perdew-Burke-Ernzerhof (PBE)[50] formulation of the generalized gradient approximation (GGA). For the plane-wave basis set in the projector augmented waves (PAWs) method[51,52], an energy cutoff of 600 eV is applied. The sampling of the Brillouin zone is conducted using Gamma-centered k-point meshes. During the structural optimizations, a convergence criterion of 1×10^{-6} eV is used for the total energy, and 1×10^{-2} eV/Å is applied for the atomic forces. To minimize interactions between neighboring periodic images along the out-of-plane direction of the slab model, a vacuum layer of 15 Å is introduced. The DFT-D3 method is employed to correct the van der Waals (vdW) dispersion interactions[53,54]. The Bader charge analysis is performed using the code developed by the Henkelman group[55]. The climbing image nudged elastic band (CI-NEB) calculations are executed with the VASP transition state theory (VTST) code[56,57].

COMSOL simulation

A symmetric cell model was used to simulate the ion flux and electric field distribution at the interface between anode and electrolyte based on COMSOL Multiphysics software[58–62]. In the 8×9 µm^2 2D geometry models (Fig. S14), the top side was the simplified electrode,the where the Mg^{2+} dissolves into the electrolyte, and the bottom area was the Mg metal electrode with an ionic insulating passivation layer or a pencil-drawn graphite-based layer. In the modeling deposition process, the whole system is filled with liquid electrolyte with an initial Mg^{2+} concentration of 500 mol m^{-3}, and the applied average current density is 1.0 mA cm^{-2}. The voltage hysteresis from symmetric cells was set as cathodic potential and the anodic potential was a constant of 0.

Data availability

All data are available from the corresponding author upon request.

References

1. Liang, Y. et al. Current status and future directions of multivalent metal-ion batteries. *Nat. Energy* **5**, 1646–1656 (2020).
2. Li et al. Cation replacement method enables high-performance electrolytes for multivalent metal batteries. *Nat. Energy* **9**, 285–297 (2024).
3. Eng, A. Y. S. et al. Theory-guided experimental design in battery materials research. *Sci. Adv.* **8**, eabm2422 (2022).
4. Hou, S. et al. Solvation sheath reorganization enables divalent metal batteries with fast interfacial charge transfer kinetics. *Science* **374**, 172–178 (2021).
5. Yang, G. et al. Realizing horizontal magnesium platelet deposition and suppressed surface passivation for high-performance magnesium metal batteries. *Energy Environ. Sci.* **17**, 1141 (2024).
6. Zhao, W. et al. Tailoring coordination in conventional ether-based electrolytes for reversible magnesium-metal anodes. *Angew. Chem.* **62**, e202205187 (2022).
7. Spotte-Smith, E. W. C. et al. Chemical reaction networks explain gas evolution mechanisms in Mg-Ion batteries. *J. Am. Chem. Soc.* **145**, 12181–12192 (2023).
8. Xiao, J. et al. Stable solid electrolyte interphase in situ formed on magnesium-metal anode by using a perfluorinated alkoxide-based all-magnesium salt electrolyte. *Adv. Mater.* **34**, 2203783 (2022).
9. Sun, Y. et al. Non-nucleophilic electrolyte with non-fluorinated hybrid solvents for long-life magnesium metal batteries. *Energy Environ. Sci.* **16**, 265–274 (2023).
10. Zhang, D. et al. Constructing efficient $Mg(CF_3SO_3)_2$ electrolyte via tailoring solvation and interface chemistry for high-performance rechargeable magnesium batteries. *Adv. Energy Mater.* **13**, 2301795 (2023).
11. Liang, Z. & Ban, C. Strategies to enable reversible magnesium electrochemistry: From electrolytes to artificial solid-electrolyte interphases. *Angew. Chem.* **60**, 11036–11047 (2021).
12. Zhang, J. et al. The origin of anode-electrolyte interfacial passivation in rechargeable Mg-metal batteries. *Energy Environ. Sci.* **16**, 1111–1124 (2023).
13. Wang, F. et al. Solvent molecule design enables excellent charge transfer kinetics for a magnesium metal anode. *ACS Energy Lett.* **8**, 780–789 (2022).
14. Liu, G. et al. Hydrated eutectic electrolytes stabilizing quasi-underpotential Mg plating/stripping for high-voltage Mg batteries. *Angew. Chem.* **62**, e202217945 (2023).
15. He, S., Luo, J. & Liu, T. L. $MgCl_2/AlCl_3$ electrolytes for reversible Mg deposition/stripping: electrochemical conditioning or not? *J. Mater. Chem. A* **5**, 12718–12722 (2017).
16. Leong, K. W. et al. Reversibility of a high-voltage, Cl^--regulated, aqueous mg metal battery enabled by a water-in-salt electrolyte. *ACS Energy Lett.* **8**, 2657–2666 (2022).
17. Xu, Y. et al. Solid electrolyte interface regulated by solvent-in-water electrolyte enables high-voltage and stable aqueous Mg-MnO_2 batteries. *Adv. Energy Mater.* **12**, 103352 (2022).
18. Horia, R., Nguyen, D. T., Eng, A. Y. S. & Seh, Z. W. Using a chloride-free magnesium battery electrolyte to form a robust anode-electrolyte nanointerface. *Nano Lett.* **21**, 8220–8228 (2021).
19. Aurbach, D. et al. Prototype systems for rechargeable magnesium batteries. *Nature* **407**, 724–727 (2020).
20. Kang, S. J. et al. Electrolyte additive enabling conditioning-free electrolytes for magnesium batteries. *ACS Appl. Mater. Interfaces* **11**, 517–524 (2019).
21. Fan, H. et al. Simultaneous optimization of solvation structure and water-resistant capability of $MgCl_2$-based electrolyte using an additive combination of organic and inorganic lithium salts. *Energy Storage Mater.* **51**, 873–881 (2022).
22. Son, S. B. et al. An artificial interphase enables reversible magnesium chemistry in carbonate electrolytes. *Nat. Chem.* **10**, 532–539 (2018).
23. Zhao, Y. et al. A bismuth-based protective layer for magnesium metal anode in noncorrosive electrolytes. *ACS Energy Lett.* **7**, 2594–2601 (2021).
24. Xiang, Y. et al. Gas induced formation of inactive Li in rechargeable lithium metal batteries. *Nat. Commun.* **14**, 177 (2023).

25. Xu, G. et al. The formation/decomposition equilibrium of LiH and its contribution on anode failure in practical lithium metal batteries. *Angew. Chem.* **60**, 7770–7776 (2021).
26. Shadike, Z. et al. Identification of LiH and nanocrystalline LiF in the solid-electrolyte interphase of lithium metal anodes. *Nat. Nanotechnol.* **16**, 549–554 (2021).
27. Fang, C. et al. Quantifying inactive lithium in lithium metal batteries. *Nature* **572**, 511–515 (2019).
28. Zhang, H., Ju, S., Xia, G. & Yu, X. Identifying the positive role of lithium hydride in stabilizing Li metal anodes. *Sci. Adv.* **8**, eabl8245 (2023).
29. Kim, J. et al. Designing fluorine-free electrolytes for stable sodium metal anodes and high-power seawater batteries via SEI reconstruction. *Energy Environ. Sci.* **15**, 4109–4118 (2022).
30. Qin, B. et al. Sodium hydride inspired the clarification of the ether-carbonate solvent disparity in sodium metal anodes. *Energy Storage Mater.* **61**, 102891 (2023).
31. Yang, C. et al. H_2O-boosted Mg-proton collaborated energy storage for rechargeable Mg-metal batteries. *Adv. Energy Mater.* **12**, 2201718 (2022).
32. Shao, Y. et al. Drawing a soft interface: An effective interfacial modification strategy for Garnet-type solid-state Li batteries. *ACS Energy Lett.* **3**, 1212–1218 (2018).
33. Tai, Z. et al. Ultra-light and flexible pencil-trace anode for high performance potassium-ion and lithium-ion batteries. *Green. Energy Environ.* **2**, 278–284 (2017).
34. Li, Z. et al. Pencil drawing stable interface for reversible and durable aqueous zinc-ion batteries. *Adv. Funct. Mater.* **30**, 2006495 (2020).
35. Song, Z. et al. Uniform magnesium electrodeposition via synergistic coupling of current homogenization, geometric confinement, and chemisorption effect. *Adv. Mater.* **33**, 2100224 (2021).
36. Chen, T., Gautam, G. S. & Canepa, P. Ionic transport in potential coating materials for Mg batteries. *Chem. Mater.* **31**, 8087–8099 (2019).
37. Li, G. et al. Locking active Li metal through localized redistribution of fluoride enabling stable Li-metal batteries. *Adv. Mater.* **35**, 2207310 (2023).
38. Wang, A., Xue, L., Guo, L., Peng, C. & Luo, J. Gradient perovskite ionic-electronic heterointerphases for deep cycling Mg metal anodes. *Adv. Funct. Mater.* **32**, 2208735 (2022).
39. Li, Y. et al. MXene-based anode-free magnesium metal battery. *Adv. Funct. Mater.* **33**, 2303067 (2023).
40. Li, Y. et al. High utilization of composite magnesium metal anodes enabled by a magnesiophilic coating. *Nano Lett.* **22**, 6808–6815 (2022).
41. Yang, G. et al. In situ formed magnesiophilic sites guiding uniform deposition for stable magnesium metal anodes. *Nano Lett.* **22**, 9138–9146 (2022).
42. Li, Y. et al. Grain-boundary-rich triphasic artificial hybrid interphase toward practical magnesium metal anodes. *Adv. Funct. Mater.* **33**, 2210639 (2022).
43. Zhang, D. et al. Borohydride-based interphase enabling reversible magnesium metal anode in conventional electrolytes. *ACS Energy Lett.* **9**, 2685–2695 (2024).
44. Zhang, Y. et al. Defect-Free Metal-Organic Framework Membrane for Precise Ion/Solvent Separation toward Highly Stable Magnesium Metal Anode. *Adv. Mater.* **34**, 2108114 (2022).
45. Bae, J. et al. High-performance magnesium metal batteries via switching the passivation film into a solid electrolyte interphase. *Energy Environ. Sci.* **14**, 4391–4399 (2021).
46. Jeon, A. R. et al. Reversible magnesium metal cycling in additive-free simple salt electrolytes enabled by spontaneous chemical activation. *ACS Nano* **17**, 8980–899 (2023).
47. Kohn, W. & Sham, L. J. Self-consistent equations including exchange and correlation effects. *Phys. Rev.* **140**, A1133–A1138 (1965).
48. Kresse, G. & Furthmuller, J. Efficient iterative schemes for ab initio total-energy calculations using a plane-wave basis set. *Phys. Rev. B* **54**, 11169–11186 (1996).
49. Kresse, G. & Furthmüller, J. Efficiency of ab-initio total energy calculations for metals and semiconductors using a plane-wave basis set. *Comput. Mater. Sci.* **6**, 15–50 (1996).
50. Perdew, J. P., Burke, K. & Ernzerhof, M. Generalized gradient approximation made simple. *Phys. Rev. Lett.* **77**, 3865–3868 (1996).
51. Blöchl, P. E. Projector augmented-wave method. *Phys. Rev. B* **50**, 17953–17979 (1994).
52. Kresse, G. & Joubert, D. From ultrasoft pseudopotentials to the projector augmented-wave method. *Phys. Rev. B* **59**, 1758–1775 (1999).
53. Grimme, S., Antony, J., Ehrlich, S. & Krieg, H. A consistent and accurate ab initio parametrization of density functional dispersion correction (DFT-D) for the 94 elements H-Pu. *J. Chem. Phys.* **132**, 154104 (2010).
54. Grimme, S., Ehrlich, S. & Goerigk, L. Effect of the damping function in dispersion corrected density functional theory. *J. Comput. Chem.* **32**, 1456–1465 (2011).
55. Henkelman, G., Arnaldsson, A. & Jónsson, H. A fast and robust algorithm for Bader decomposition of charge density. *Comput. Mater. Sci.* **36**, 354–360 (2006).
56. Henkelman, G. & Jónsson, H. Improved tangent estimate in the nudged elastic band method for finding minimum energy paths and saddle points. *J. Chem. Phys.* **113**, 9978–9985 (2000).
57. Henkelman, G., Uberuaga, B. P. & Jónsson, H. A climbing image nudged elastic band method for finding saddle points and minimum energy paths. *J. Chem. Phys.* **113**, 9901–9904 (2000).
58. Zhang, C. et al. An electron-blocking interface for garnet-based quasi-solid-state lithium-metal batteries to improve lifespan. *Nat. Commun.* **15**, 5325 (2024).
59. Ishikawa, K., Fujima, N. & Komura, H. First-order Raman scattering in MgO microcrystals. *J. Appl. Phys.* **57**, 973–975 (1985).
60. Dawson, P., Hadfield, C. D. & Wilkinson, G. R. The polarized infra-red and Raman spectra of $Mg(OH)_2$ and $Ca(OH)_2$. *J. Phys. Chem. Solids* **34**, 1217–1225 (1973).
61. Li, Y. et al. Hybrid polymer-alloy-fluoride interphase enabling fast ion transport kinetics for low-temperature lithium metal batteries. *ACS Nano* **17**, 19459–19469 (2023).
62. Li, G. et al. Catalytic anode surface enabling in situ polymerization of gel polymer electrolyte for stable Li metal batteries. *Nano Res.* **17**, 5216–5223 (2024).

Acknowledgements

Z. W. S. acknowledges the Singapore National Research Foundation (NRF Investigatorship NRF-NRFI09-0002) and the Agency for Science, Technology and Research (MTC Programmatic Fund M23L9b0052 and Central Research Fund Award). M.-F. N. acknowledge the National Supercomputing Center (NSCC) Singapore and A*STAR Computational Resource Center (A*CRC) of Singapore through the use of its high-performance computing facilities.

Author contributions

Y.L., J.L., and Z.W.S. conceived the project. Y. L. prepared the samples and performed the structural characterizations and electrochemical measurements. G. Y., W. Y. L., L. Fu., and Z. X. helped with structural characterizations. X. F., Q. Z., and M.-F. N., performed the DFT calculations and analysis. C. Z. and W. L. performed the COMSOL simulations and analysis. Y.L., J.L., and Z.W.S. wrote and edited the manuscript. All authors analyzed the results and commented on the manuscript.

Competing interests

The authors declare no competing interests.

Additional information

Supplementary information The online version contains supplementary material available at https://doi.org/10.1038/s41467-024-53796-z.

Correspondence and requests for materials should be addressed to Wei Liu, Jun Lu or Zhi Wei Seh.

Peer review information *Nature Communications* thanks Robert Dominko and the other, anonymous, reviewers for their contribution to the peer review of this work. A peer review file is available.

Reprints and permissions information is available at http://www.nature.com/reprints

Publisher's note Springer Nature remains neutral with regard to jurisdictional claims in published maps and institutional affiliations.

Open Access This article is licensed under a Creative Commons Attribution-NonCommercial-NoDerivatives 4.0 International License, which permits any non-commercial use, sharing, distribution and reproduction in any medium or format, as long as you give appropriate credit to the original author(s) and the source, provide a link to the Creative Commons licence, and indicate if you modified the licensed material. You do not have permission under this licence to share adapted material derived from this article or parts of it. The images or other third party material in this article are included in the article's Creative Commons licence, unless indicated otherwise in a credit line to the material. If material is not included in the article's Creative Commons licence and your intended use is not permitted by statutory regulation or exceeds the permitted use, you will need to obtain permission directly from the copyright holder. To view a copy of this licence, visit http://creativecommons.org/licenses/by-nc-nd/4.0/.

© The Author(s) 2024